

Satellite Manoeuvre Detection and Analyses Based on Ephemerides

Wenze Ma ^a, Qiangyi Huang ^a, Yang Yang ^b

^a School of Electrical Engineering and Telecommunications, The University of New South Wales, Australia

^b School of Mechanical and Manufacturing Engineering, The University of New South Wales, Australia

* Corresponding Author: Yang Yang (e-mail: yang.yang16@unsw.edu.au)

Abstract

With the development of mega constellation, robust law and criteria of satellite manoeuvre are required by the new generation of integrated control method among satellites to perform better conjunction and collision avoidance with high precision as the quantity grows. The precise time epoch and orbital performance of low thrust manoeuvres with subtle altitude change have been detected and analysed based on the ephemerides of about 7,000 Starlink satellites from September 2024. The development and deorbiting manoeuvres have been identified from the change of semi-major axis, which is coincident with the official record. For station-keeping manoeuvres with imperceptible variation and frequent operation, the algorithm focusing on the adjacent valley value of mean semi-major axis vibration in the precision of 50 metres has been applied to satellites grouped by the launch, detecting the duration and altitude change of the true manoeuvres from the anomalies, with validation attempted by the covariance from the operator and the machine learning method.

Keywords: Satellite, Manoeuvre, Space Situational Awareness, Starlink, LEO

Nomenclature

e = eccentricity

i = inclination

Ω = the ascending node

ω = the argument of perigee

θ = the true anomaly

a = semi-major axis

w = moving window size

Λ = Poincare action associated with the semi-major axis

ξ = sine component of the Poincare eccentricity coordinate

η = cosine component of the Poincare eccentricity coordinate

u = sine component of the Poincare inclination coordinate

v = cosine component of the Poincare inclination coordinate

λ = mean longitude

North American Aerospace Defense Command

(NORAD)

Density-based spatial clustering of applications with noise (DBSCAN)

Earth Gravitational Model (EGM)

National Geospatial-Intelligence Agency (NGA)

1. Introduction

With the growing need of telecommunication interaction, LEO satellites are preferred to conduct space missions of Internet communication with large coverage area and fast response due to the low value of signal delay and less manufacture cost comparing with satellites in higher orbits such as GEO and MEO [1]. Permitted by the FCC, the mega constellation structure of Starlink is planned in two generations, including 7 shells of around 12,000 LEO satellites with different orbital height [2, 3, 4]. By August 2025, 8,298 satellites were in operation from the total launched of 9,580, some of which were driven to re-enter to the Earth atmosphere or redirected to the desired orbit due to the unexpected functional loss [5]. With more space mission of LEO satellites deployed, the limited LEO region would be crowded with potential collision and complicated launch window considering the density of satellites in the certain orbit. From the perspective of SSA and SDA, precisely tracking and timely operating satellites to avoid these hazards are required [6].

For functional LEO satellites in orbits lower than 750 km, manoeuvres should be executed following the configuration-based control method against the orbital decay generated by the perturbation including gravitational force, atmospheric drag and J2 effect [7, 8]. From the separation with the rideshare platform to the re-entry at the end of mission lifetime, low-thrust

Acronyms/Abbreviations

Ephemerides (EPH)

Classical orbital element (COE)

Low Earth orbit (LEO)

Geostationary orbit (GEO)

Medium Earth orbit (MEO)

Federal Communication Commission (FCC)

Space situational awareness (SSA)

Space domain awareness (SDA)

Two-line element (TLE)

Kalman filter (KF)

Extended Kalman filter (EKF)

Long short-term memory (LSTM)

Semi-major axis (SMA)

Machine learning (ML)

manoeuvres would be classified as types of deployment, station-keeping, collision-avoidance, and deorbiting according to the mission in different phases.

Recently, the manoeuvre detection and prediction have been conducted based on two types of data. Orbital mechanism model with filters such as optimal proposal particle filter and bootstrap particle filter have been implemented to detect anomalies in the operation of satellites based on TLE [7, 9, 10]. Since most manoeuvres of Starlink satellites are accomplished by the electrical propulsion system, providing continuous and low impulse, the altitude change would be in the unit of cm/s, which is scaled down from the large-thrust manoeuvre in the unit of m/s [11]. EPH with higher precision and more frequent update of satellite performance would fit with advanced filtering algorithm such as EKF and LSTM to reduce the vibration and extract the anomalous pattern of orbital performance [12, 13].

Although types of manoeuvres are classified, the time epoch and altitude change are not provided, which should be defined for satellites in different orbits conducting the specific type of manoeuvre, especially the most frequent station-keeping manoeuvre. With the exact duration and trajectory of the manoeuvre noticed, attitude adjustments and the deployment window can be designed in advance to avoid potential collision among existed satellites and launching objects respectively from different operators.

This paper focuses on the manoeuvre detection of satellites grouped by the launch date, providing detailed performance of deployment, deorbiting, and station-keeping manoeuvres as reference for future operation of mega constellation in the crowded LEO region based on the EPH data of 10 months from September 2024. The high-pass filter focusing on the adjacent peak values of the SMA is proposed, distinguishing the deployment and deorbiting manoeuvres of satellites in the dataset. The result is compared and validated by the operational record of launched and re-entered satellites. The exact start and end time of the station-keeping manoeuvre with the altitude change are regulated by intersections between the line functions fit from the non-manoeuvre and manoeuvre data identified by the difference between adjacent valley values of mean SMA processed by the moving-average filter of every 91 minutes. Since there is no operational record of the detailed manoeuvre performance, validation is attempted by methods including the confidence coverage using covariance extracted from the EPH, other orbital elements, *i.e.*, Poincare variables, and clustering of orbital raises by the unsupervised ML.

The structure of the paper is organized as follows. The dataset of EPH is introduced in Section 2. Section 3 illustrates the data pre-processing, including the coordinate conversion, overlap duplication, error elimination, and smoothing from large-scale

oscillations. The frameworks of algorithms detecting deployment, deorbiting, and station-keeping manoeuvres with validation results are presented in Section 4. Instead of focusing on single object, the detection results among satellites from the same launch group is compared in Section 5 with future perspectives discussed.

2. Dataset introduction

As of July 28, 2025, the available satellite data had been sourced from Starlink EPH reposted by the Space-Track organization [14]. After this date, the data source was changed to the official Starlink website, and the team suspended data collection from that date onward. The dataset began on September 10, 2024, with a gap between March and May 2025. The total dataset comprised approximately 260 updates, amounting to 6.9 TB of raw data.

On the Space-Track platform, the data update frequency was three times per day, with each update providing predictions for the subsequent three days. The data were presented in compressed packages, each containing information for 500 satellites. On average, each update consisted of approximately 14 compressed files, corresponding to about 7,000 satellites distributed in the orbit of 300 to 600 km as shown in Fig. 1, and amounted to roughly 15 GB of data. Missing satellite data in certain updates were supplemented in the subsequent one or two updates, occasionally resulting in more than 20 compressed packages per update, which implied that the data volume could exceed 20 GB.

For an individual satellite, the data was stored in the ITC format [15] as shown in Fig. 2. The first four lines introduce the basic information of satellites, including the NORAD ID and the start and end times of the current update. Beginning from the fifth line, repeating cycles of every four lines provide the epoch, position and velocity vectors in the first line, followed by the lower 6×6 triangular covariance matrix of position and velocity in the satellite-centred UVW reference frame, where U represents the direction from Earth to satellite, V represents the direction perpendicular to the U direction and the velocity vector, W represents the direction of satellite's velocity vector [15].

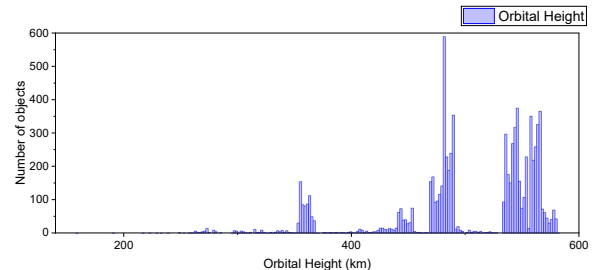


Fig. 1. Altitude distribution of satellites in the dataset

```

created:2024-09-13 04:34:01 UTC
ephemeris_start:2024-09-13 00:12:42 UTC ephemeris_stop:2024-09-16 00:12:42 UTC step_size:60
ephemeris_source:blend
UVW
2024257001242.000 1465.6423224945 -5076.3899013023 -4093.1412221437 4.7698379855 4.5874710123 -3.9779673718
7.4401763503e-07 -3.8600829909e-07 7.6646638270e-07 -1.1821781929e-09 2.0485437879e-10 1.1279136549e-06 1.2701998168e-09
-9.4971617105e-10 -3.0820724342e-12 2.7285159644e-12 -4.6347223125e-10 3.9143409177e-10 1.2469265787e-12 -8.1455559469e-13
5.2289897369e-13 -2.5935499007e-12 -4.6684381459e-13 1.5198468375e-09 -5.0129597448e-15 1.0328442756e-15 5.6615530719e-12
2024257001342.000 1748.0880972002 -4789.1843511097 -4321.7801769800 4.6412567132 4.9821939885 -3.6402842174
8.4832141407e-07 -4.7681109158e-07 8.7737247244e-07 -1.5130405439e-09 4.0557197506e-10 1.3246874863e-06 1.4656218576e-09
-1.1367216965e-09 -3.8971863296e-12 3.1157122955e-12 -5.4143729657e-10 4.6523534450e-10 1.6953483974e-12 -9.6551595653e-13
5.7837761363e-13 -3.3043780918e-12 1.1830341826e-13 1.7547187058e-09 -6.4985124270e-15 1.9335655262e-15 5.4279940169e-12

```

Fig. 2. Example of the downloaded data

3. Data pre-processing

Data pre-processing included converting the raw EPH data into a standardized format, filtering and removing anomalous values, and applying multiple smoothing techniques such as the KF, the moving average filter, and the peak filter. The primary objective of this process was to transform the EPH data into more intuitive and widely used orbital parameters, thereby facilitating the observation of variations associated with orbital manoeuvres.

3.1 Data coordination conversion

The pre-processing of the dataset consisted of converting the existing satellite ephemerides into more direct and intuitive Keplerian orbital elements. The implemented program could search all available ephemerides corresponding to a given satellite identifier within the dataset. Without decompressing the archive files containing the data, the program read and processed the relevant records, thereby generating the corresponding Keplerian elements for each epoch.

An example is shown in Fig. 4, which illustrated 6COEs of satellite No. 61050 derived from the available dataset. Some gaps indicate the missing data because of the technical failure in download. The dense region with repeated data caused by the multiple updates will be depicted in Section 3.2 with the time-based filter implemented. Outliers are recognized as data error happen along the prediction and will be processed in Section 3.3. As some orbital elements such as SMA fluctuate in large amplitude frequently for every orbital period, the oscillation would be scaled down in Section 3.4, detecting imperceptible manoeuvre signatures.

After obtaining the classical Keplerian orbital elements, they could be transformed into alternative sets of orbital parameters, such as the Poincare variables, for further analysis. The transformation equations are given as follows [16]. The Poincare variables are characterized by their non-singular behaviour: they remain continuous in the limiting cases of $e \rightarrow 0$ (nearly circular orbits) and $i \rightarrow 0$ (nearly equatorial orbits), thereby avoiding the classical singularities associated with ω and Ω .

Moreover, the angular dependence appears in the form of the combined angle $\omega + \Omega$, which prevents undefined conditions in these regimes.

$$\Lambda = \sqrt{\mu a} \quad (1)$$

$$\xi = e \sin(\omega + \Omega) \sqrt{2\Lambda/(1 + \sqrt{1 - e^2})} \quad (2)$$

$$\eta = e \cos(\omega + \Omega) \sqrt{2\Lambda/(1 + \sqrt{1 - e^2})} \quad (3)$$

$$u = \sin i \sin \Omega \sqrt{2\Lambda\sqrt{1 - e^2}/(1 + \cos i)} \quad (4)$$

$$v = \sin i \cos \Omega \sqrt{2\Lambda\sqrt{1 - e^2}/(1 + \cos i)} \quad (5)$$

$$\lambda = \lambda \quad (6)$$

3.2 Deduplication

The EPH from each download, containing the prediction of satellites for three days after the start time of the file, is updated by SpaceX at the frequency of about eight hours. Fig. 3 demonstrates the overlap pattern within every 3 days. It is noted that there would be up to nine datapoints at the same timestamp during the densely downloaded period, labelled as ‘day4 0h’.

The prediction error would accumulate with time, where the most precise data should be referred to the latest update from SpaceX on space-track. For less duplication and more accurate extraction at the specific time, the raw EPH was processed by the algorithm as shown in Fig. 5. The validation of whether the extracted EPH reliable was conducted by ensuring the specific time greater than the start time of the latest download since the extraction would fail if the chosen time were closer to the start time of the latter adjacent file instead of the one before. The dataset with only one precise value at the specific time was saved as the reliable EPH for the following procession.

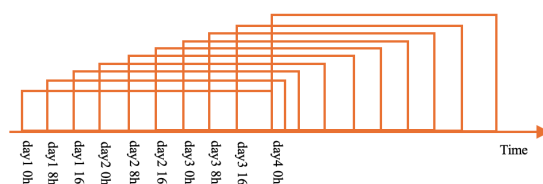


Fig. 3. Example pattern of overlap in downloaded EPH

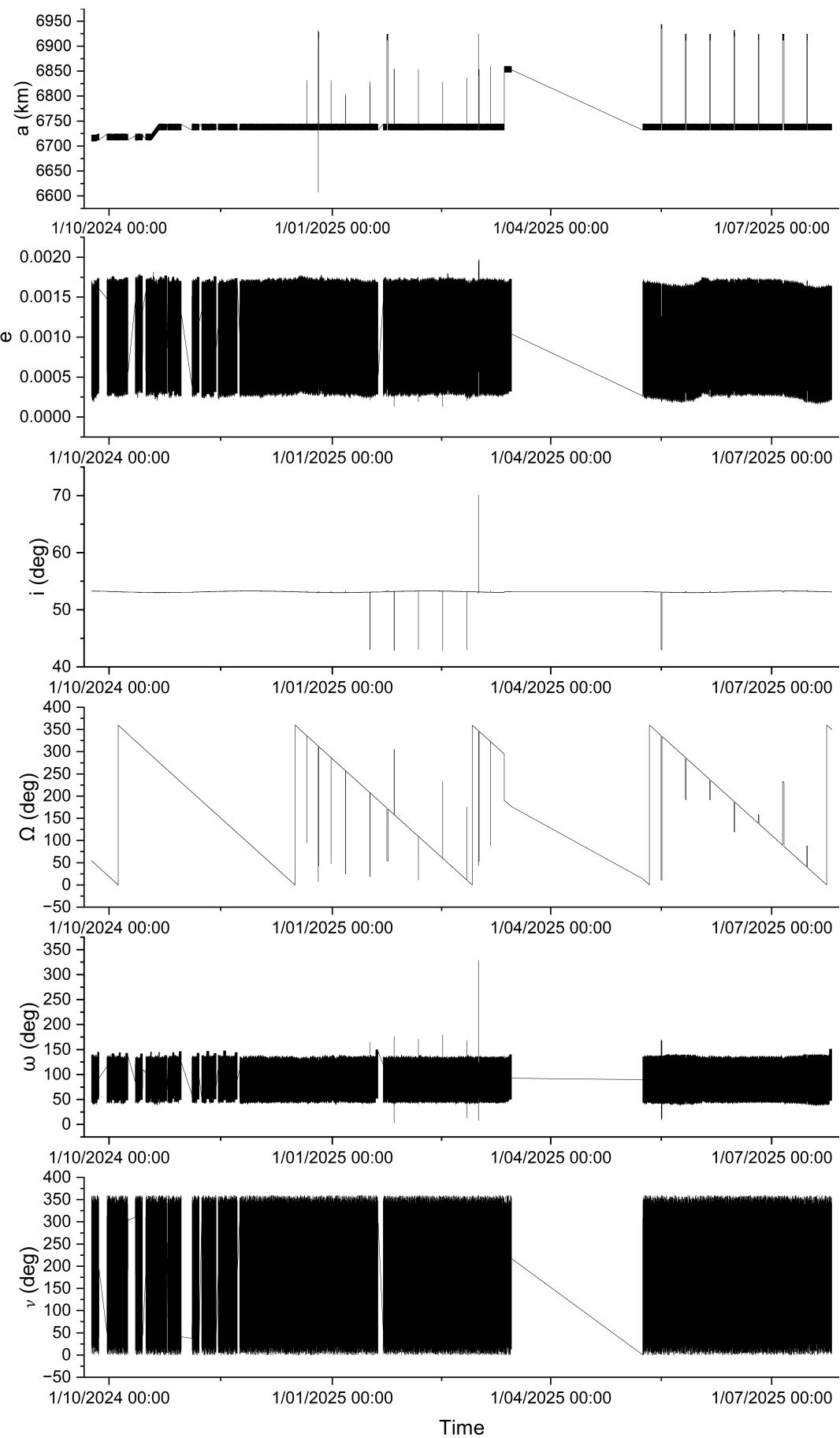


Fig. 4. 6COEs of Starlink satellite #61050

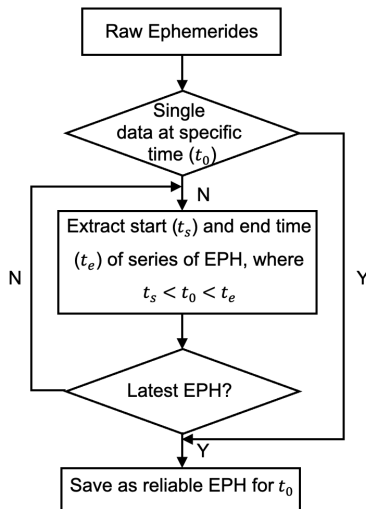


Fig. 5. Logic of data deduplication

3.3 Abnormal data handling

Although EPH provides precise prediction of the satellite performance, some data error of specific orbital elements (for example, SMA used) would

happen due to the drift-off of either the position or velocity vectors. As shown in the top subfigure of Fig. 4, there are several protrusions out of the curve of the raw SMA without overlap for Starlink satellite #61050. These visual anomalies, indicating the satellite has accomplished orbital raising over 150 km within a few minutes, which is impossible for the low-thrust manoeuvre and should be excluded from the dataset.

Since these data errors are hard to be positioned and removed manually, a high-pass filter was desired with universal thresholds which could be implemented for other satellites. Points labelled in blue and green as shown in Fig. 6 represent the largest and lowest value of SMA in each orbital decay with detailed information introduced in Table 1. For normal orbital vibration, the adjacent peak and valley has a difference lower than 0.05% of the valley value, on which the threshold tuning was based. All adjacent SMA with the difference greater than threshold should be recognized as outliers and deleted. The algorithm of the data anomaly elimination is introduced as shown in Fig. 7. Due to the structure of the dataset, periods of missing data should be ignored and kept the empty format.

Table 1. Data of peak and valley SMA

| Peak SMA(km) | Valley SMA(km) | (Peak-Valley)/Valley |
|--------------|----------------|----------------------|
| 6739.67453 | 6736.62918 | 0.000452058 |
| 6739.67970 | 6736.68688 | 0.000444257 |
| 6739.58310 | 6736.58911 | 0.000444437 |
| 6739.57003 | 6736.58995 | 0.000442372 |
| 6739.66594 | 6736.68033 | 0.000443187 |
| 6739.61698 | 6736.64918 | 0.000440545 |
| 6739.61118 | 6736.61841 | 0.000444254 |

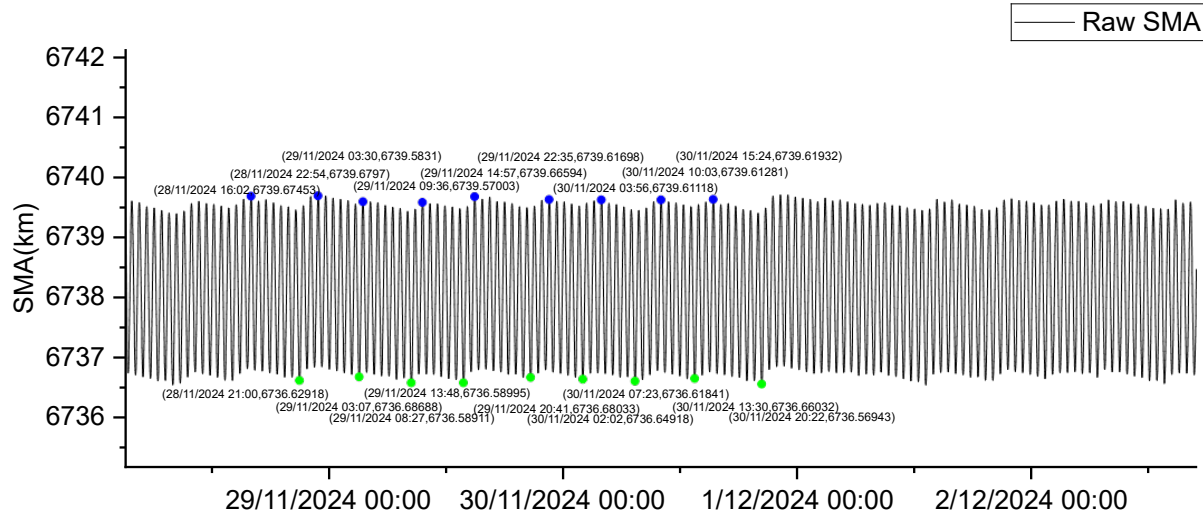


Fig. 6. Normal oscillation example

To ensure the continuity of the dataset, anomalous data points could also be addressed by replacing them with previously valid records or by interpolating values based on the surrounding data. After the erroneous data being identified and verified, the valid

data accepted by the threshold would be chosen among the overlapped dataset as replacement.

In subsequent large-scale analyses, anomalies were typically handled by removing erroneous points and reconstructing them through interpolation using neighbouring data. This method effectively improved

the continuity of the dataset and enhanced processing efficiency. However, in terms of reliability, it was less robust than the first approach, and in practice, the use of interpolated values could reduce the accuracy in manoeuvre detection.

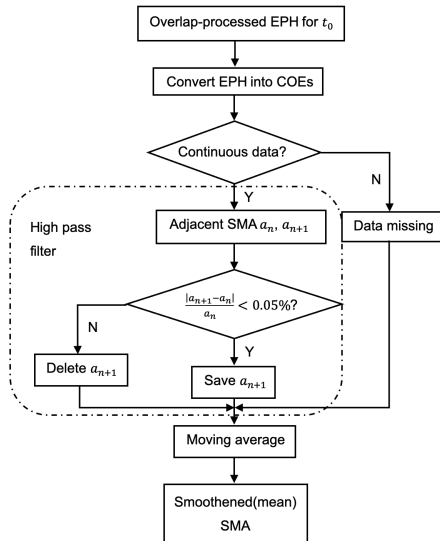


Fig. 7. Logic of the error elimination

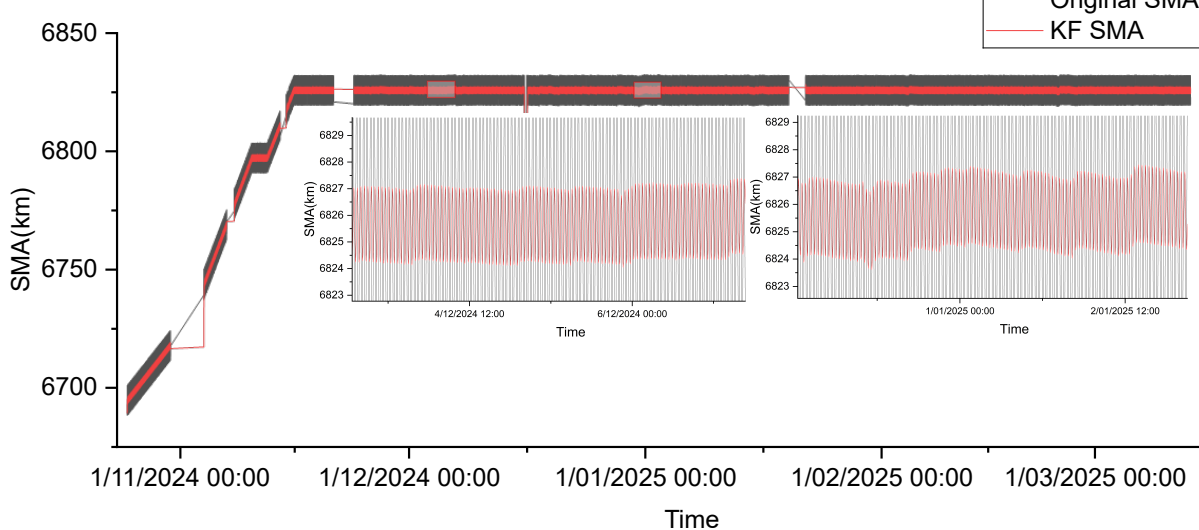


Fig. 8. Original SMA vs. KF-processed SMA of Starlink satellite #61510

3.4.2 Peak-only

To emphasize the pattern of orbital raises, only peak values of the processes SMA were extracted as shown in Fig. 9. It would be a waste to use discontinuous data instead of the timestamp with the precision of every minute since the peak would occur every 22 to 23 minutes.

3.4 Data smoothening

Since the orbital height encoded from the EPH would oscillate around 15 km in every orbital period instead of the theoretically constant assumption for LEO satellites, the amplitude of the oscillation should be reduced with the trend of orbital rises and decays emphasised, especially for the station-keeping manoeuvre. The smoothening process was tested by three filters, from which the moving-average method with the window size of 91 minutes was selected.

3.4.1 Simple Kalman Filter

Considering the aim of data smoothening was focused on the SMA of satellites, the processed SMA data without overlap and error was decided as the input of the 1D simple Kalman Filter instead of the state vectors. The noise variance, which defines the extent of the amplitude concentration, was tuned as 0.01 for the initial guess. A fixed value of 10 was defined as the uncertainty of the smoothed data. As shown in Fig. 8, the amplitude of oscillation is reduced to about 2.5 km from 15 km, which is desired to be further scaled down for station-keeping manoeuvres with smaller altitude change.

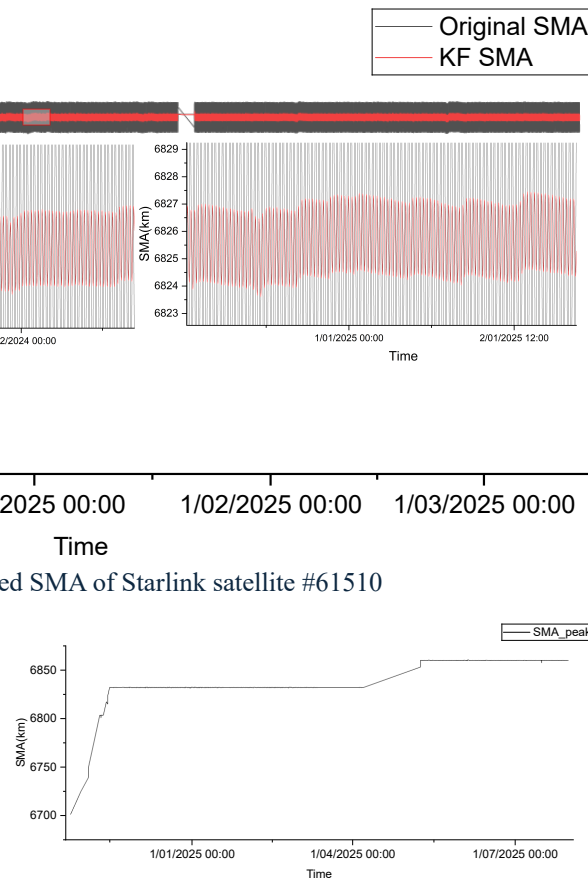


Fig. 9. Peaks of the original SMA of Starlink satellite #61510

3.4.3 Moving average

The conventional mean orbital elements are processed by excluding the first- and second-order

solutions of non-singular elements with the gravitational field of a certain range from the original ones [17]. Since the raw SMA was encoded from the EPH, it was not acceptable to directly removing the longitude-related noise from the spherical harmonics. After introducing the J_2 parameter by expanding the 20th order EGM 2008 downloaded from NGA [18, 19] using Taylor series expansion, the first- and second-order correction of the SMA is introduced as shown.

$$\Delta a^{(1)} = \frac{3}{2} \cdot J_2 \cdot \frac{R_E^2}{a(1-e^2)^2} \cdot (1 - \frac{3}{2} \cdot \sin^2 i) \cdot a \quad (7)$$

$$\Delta a^{(2)} = -\frac{3}{4} \cdot \left(\frac{J_2 \cdot R_E^2}{a(1-e^2)^2}\right)^2 \cdot (1 - \frac{3}{2} \cdot \sin^2 i)^2 \cdot a \quad (8)$$

$$a^{(1)}_{mean} = a - \Delta a^{(1)} \quad (9)$$

$$a^{(2)}_{mean} = a - \Delta a^{(1)} - \Delta a^{(2)} \quad (10)$$

The result turns out that the first-order corrected SMA was reduced to around 4,000 km from 6,700 km with the amplitude of the vibration increased to about 30 km, which is not desired. The second-order correction would fit the potential energy since the negative coefficient led to more frequent oscillation of the mean SMA. The position and velocity vectors should be processed with the first-order correction before being converted into COEs.

The method of moving average was implemented alliteratively by calculating the mean value of SMA within each observation window as shown below. The window size was initially decided as 91 minutes which is aligned with the orbital period of LEO satellites. For the chosen timestamp, the mean SMA value was extracted from every 91 points as shown in Fig. 10. As shown in Fig. 11, the amplitude of the orbital oscillation was reduced to around 1 km with the precision of every minute, which meets the requirement of manoeuvre detection.

$$\bar{a}_i = \frac{1}{w} \sum_{j=i-(w-1)/2}^{i+(w-1)/2} a_j \quad (11)$$

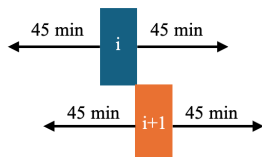


Fig. 10. Moving window

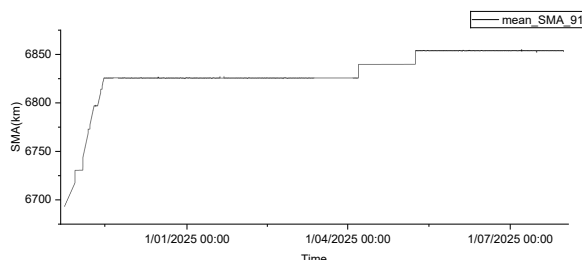


Fig. 11. Mean SMA of Starlink satellite #61510

4. Manoeuvre detection algorithm and results

The detection of orbital manoeuvres was classified into three categories: deorbiting, deployment, and station keeping. The first two categories, which corresponded to long-duration and large-scale manoeuvres, were analysed together. In contrast, the detection of station keeping manoeuvres presented greater challenges because of the subtle change in orbital height. Since no authoritative or accurate datasets were available to directly validate such operations, multiple approaches were attempted to identify indirect evidence of satellites performing station-keeping manoeuvres.

4.1 Deorbiting and deployment manoeuvre

The most distinct feature of orbital manoeuvres is the variation in the semi-major axis. Based on the semi-major axis values derived from the EPH data, the corresponding time series exhibited periodic oscillations. Consequently, the peaks and troughs associated with these oscillations were extracted, and the peak-to-peak values were calculated. In the absence of manoeuvres, the amplitudes of consecutive peak-to-peak values remained nearly constant. When a manoeuvre occurred, the differences between adjacent peaks and troughs changed. Specifically, if the first peak-to-peak value decreased while the subsequent one increased, this indicated an orbit-raising manoeuvre. Conversely, if the first peak-to-peak value increased while the subsequent one decreased, this suggested an orbit-lowering manoeuvre.

Based on these observations, a dedicated program was developed to monitor the trend of consecutive peak-to-peak variations in the semi-major axis. The program could detect whether a satellite had performed long-duration or large-scale manoeuvres, which could be categorized into two types: deployment and deorbiting. By calculating the peak-to-peak differences of all Starlink satellites over a six-day period, a set of satellites with the largest numbers of consecutive peak-to-peak differences greater than 5% was identified, as shown in Table 2. Furthermore, a scatter plot of all satellites with consecutive peak-to-peak differences exceeding 5% was generated, as illustrated in Fig. 12. The results revealed that, for most satellites exhibiting significant manoeuvres, the difference between two consecutive peak-to-peak values exceeded 5%. Therefore, a threshold of 5% in consecutive peak-to-peak differences was adopted as the criterion for manoeuvre detection.

Table 2. Ranking of peak-to-peak changes greater than 5% within 6 days

| NORAD ID | Count above 5% | Total Count |
|----------|----------------|-------------|
| 57293 | 160 | 173 |
| 48446 | 92 | 192 |
| 47570 | 90 | 192 |
| 59665 | 75 | 192 |
| 60287 | 23 | 184 |

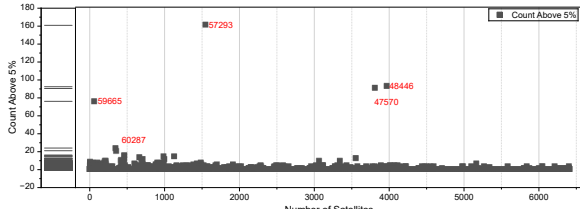


Fig. 12. Peak-to-peak changes greater than 5% within 6 days

As illustrated in Fig. 13, the semi-major axis variation of satellite No. 57293 exhibited the largest number of consecutive peak-to-peak changes within the specified time window. It is evident from the figure that satellite 57293 underwent a pronounced atmospheric re-entry process, descending from an altitude of approximately 300 km to destruction within 1,000 minutes. This observation was further validated by cross-referencing with the orbital status monitoring provided by the N2YO website [20], which confirmed that the satellite decayed on September 18, 2024. This case demonstrated that the proposed detection method was indeed capable of identifying satellites that experienced orbital decay and eventual re-entry.

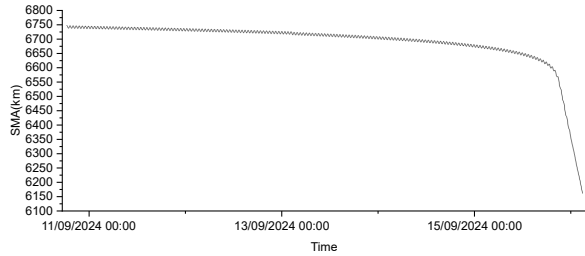


Fig. 13. SMA of deorbiting Starlink satellite #57293

As illustrated in Fig. 14, the semi-major axis variation of satellite No. 60287 clearly showed a long-duration and large-scale orbit-raising manoeuvre shortly after its launch. The manoeuvre lasted for approximately 3,000 minutes and resulted in an overall altitude increase of about 30 km. During this period, all consecutive peak-to-peak variations exceeded the 5% threshold, which was consistent with the previously defined criterion: if the first peak-to-peak value decreased while the subsequent one increased, this indicated an orbit-raising manoeuvre. By comparing it with Jonathan's website [5], it was observed that the same satellite exhibited nearly identical long-duration and large-scale orbital variations within the corresponding duration. This cross-validation further confirmed the feasibility and robustness of the proposed approach.

In summary, the program effectively identified satellite deorbiting and deployment manoeuvres by adopting a threshold of 5% in the difference between consecutive peak-to-peak values of the semi-major axis. The magnitude of these variations enabled the determination of both the occurrence and the duration of the manoeuvre. The consistency of the monitoring

results with external datasets further demonstrated the accuracy and reliability of the proposed approach.

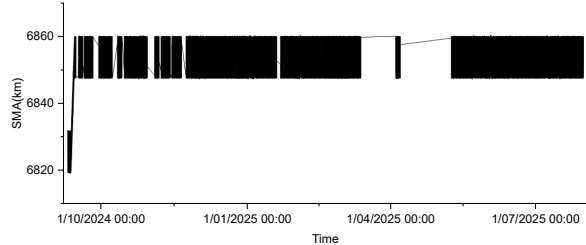


Fig. 14. SMA of deployment manoeuvre of Starlink satellite #60287

4.2 Station-keeping manoeuvre

Due to the perturbation and strong influence of atmospheric drag in the LEO environment, satellites should conduct station-keeping manoeuvres periodically against the orbital decay to guarantee the function of communication and the desired mission lifetime. Different from other types of manoeuvres, the station-keeping manoeuvre would be conducted among satellites from the same launch group with the altitude change at the level of 100 m, which should be detected by filters with higher precision [6]. The detection was tried with four different methods, defining the anomalous patterns from the mean SMA, covariance from the EPH, Poincare orbital elements by converting the coordination, and machine learning.

4.2.1 Mean SMA

The threshold of the filter detecting station-keeping manoeuvres was defined by the normal orbital decay influenced by the perturbation and atmospheric drag, shown as the red and green curves in Fig. 15. The blue and purple curves in Fig. 15 represent the orbital raises that would possibly be the desired manoeuvre pattern conducted by the thruster. Peaks and valley value of the mean SMA, labelled as blue and red respectively, is introduced in Table 3. It was found that the mean time from the valley to the peak was about 24 minutes with the difference of about 100 metres in the mean SMA. The algorithm is as shown in Fig. 17, focused on the adjacent valleys of the mean SMA. If the difference between them is greater than half of the valley-peak value, which is 50 metres, the movement should be recognized as suspected manoeuvres. (represented as the green points with their former blue points) Otherwise, it should be processed as non-manoeuvre data. To define the precise time epoch where the manoeuvre starts and ends, each set of non-manoeuvre data were fit with line functions of $f_b(t)$ and $f_a(t)$ with the set of manoeuvre data between fit as $f_m(t)$. The start (t_s) and end time (t_e) was defined as the time of the intersection between $f_b(t)$ and $f_m(t)$, and $f_m(t)$ and $f_a(t)$ respectively. The mean SMA of $f_m(t_s)$ and $f_m(t_e)$ were checked whether it was data error. If $f_m(t_e) - f_m(t_s) > 100 m$, which was the mean difference between adjacent valleys and peaks, it should be confirmed as true manoeuvre from t_s to t_e .

Table 3. Detailed adjacent peak-value difference

| Time | Valley-Peak time (min) | Mean SMA (km) | Peak-Valley SMA (m) |
|-------------|------------------------|---------------|---------------------|
| 26/11 23:22 | 23 | 6738.16848 | 104.6 |
| 26/11 23:45 | | 6738.27308 | |
| 27/11 10:47 | 26 | 6738.20382 | 100.97 |
| 27/11 11:13 | | 6738.30479 | |

By implementing the detection method, station-keeping manoeuvres should be restricted within the exact epoch. The detailed performance of the detected manoeuvres on November 27 and November 28, 2024,

is introduced in Table 4. Comparing with the defined valleys of the suspected manoeuvres, it is noted that detection would provide larger time intervals because of the offset of earlier t_s and later t_e brought by intersections of fit line functions. The cluster results as shown in Fig. 16 are designed to find the regulation of all detected station-keeping manoeuvres. The negative value represents the faster orbital decay comparing with the normal one generated by the perturbation. This movement would be the compensation of excessive orbital raise operated by the redundant propulsion of the thruster to move the satellite back into the desired lower orbit. For the orbital raises, most station-keeping manoeuvres were found accomplished within around 2 hours with the orbital altitude being rising for about 250 metres.

Table 4. Detailed performance of the detected manoeuvres

| Start time | End time | Duration (min) | Start SMA (km) | End SMA (km) | Amplitude (m) |
|------------------|------------------|----------------|----------------|--------------|---------------|
| 27/11/2024 9:04 | 27/11/2024 11:17 | 133 | 6737.95148 | 6738.29594 | 344.4599 |
| 27/11/2024 15:17 | 27/11/2024 17:15 | 118 | 6738.09183 | 6738.33947 | 247.6355 |
| 28/11/2024 8:01 | 28/11/2024 10:14 | 133 | 6737.97805 | 6738.20911 | 231.0614 |
| 28/11/2024 13:22 | 28/11/2024 15:33 | 131 | 6738.06507 | 6738.29095 | 225.8758 |
| 28/11/2024 20:14 | 28/11/2024 22:20 | 126 | 6738.06541 | 6738.32913 | 263.7288 |

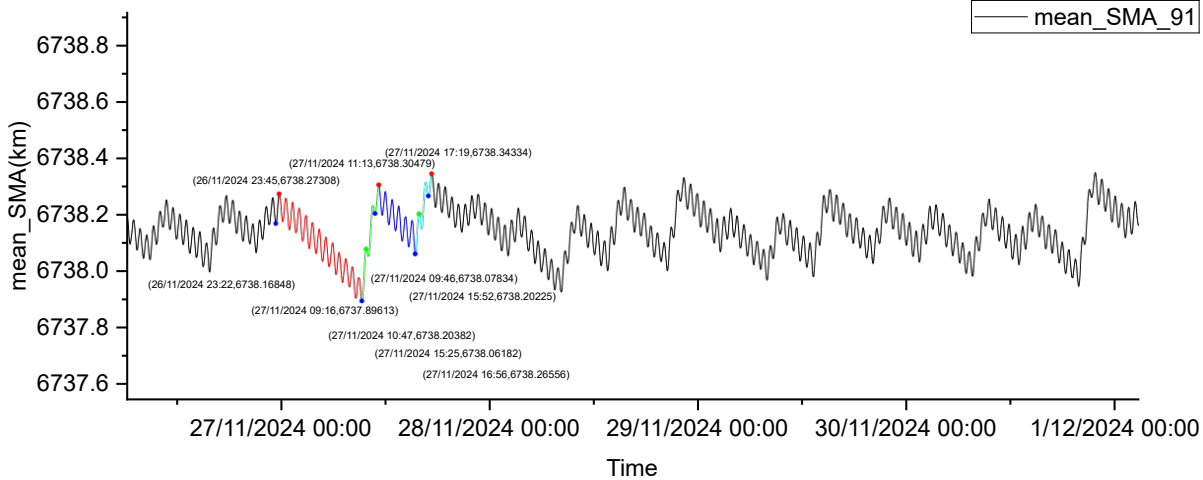


Fig. 15. Detailed orbital height oscillation of station-keeping manoeuvres

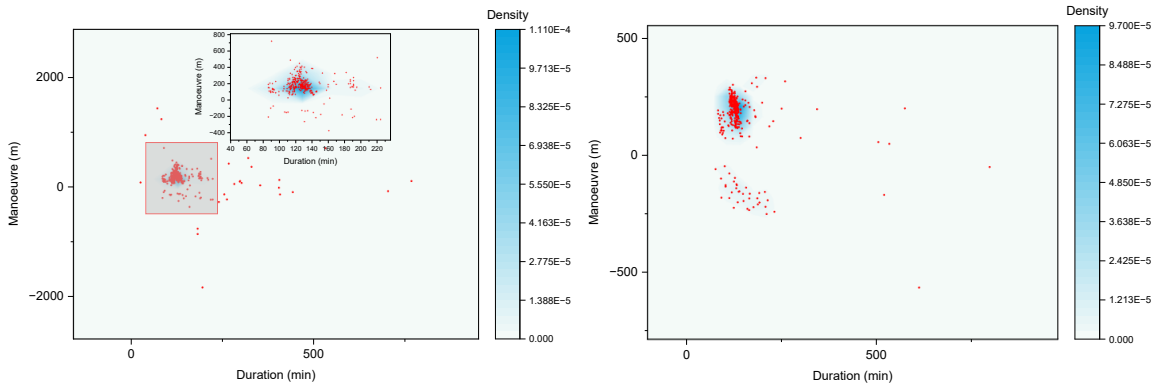


Fig. 16. Intensity plot of the detected manoeuvres of Starlink satellite #61050 (left) and #58705 (right)

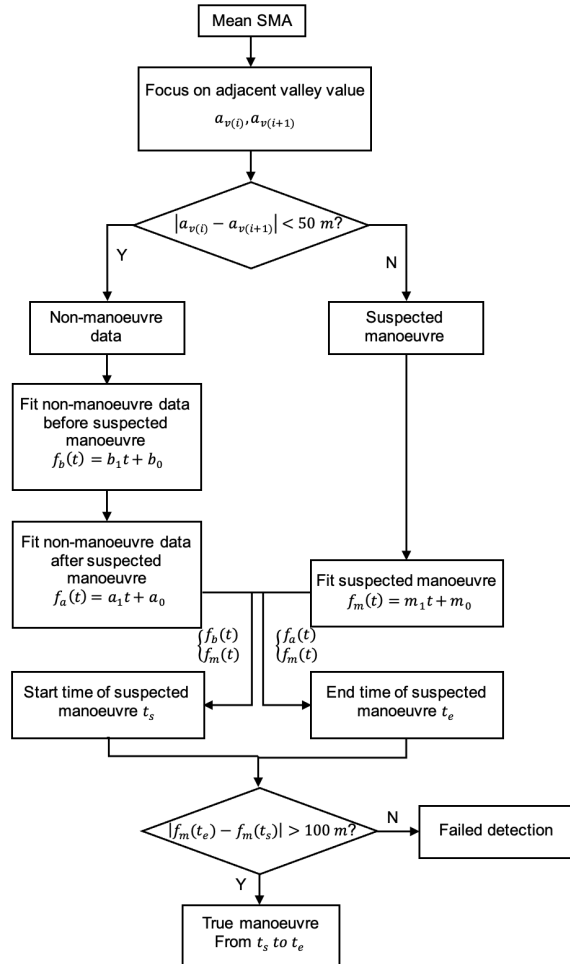


Fig. 17. Algorithm of station-keeping manoeuvres detection using the mean SMA

4.2.2 Covariance validation

According to the format of the EPH provided by SpaceX, each set of data contains the 21 elements in the lower triangle of the covariance matrix of the six components in the two state vectors. Since SMA is calculated from the EPH, the covariance of SMA should follow the same encoding process as shown below, where P is the full expansion of the covariance matrix.

$$\nabla a = \left(\frac{\partial a}{\partial x} \quad \frac{\partial a}{\partial y} \quad \frac{\partial a}{\partial z} \quad \frac{\partial a}{\partial v_x} \quad \frac{\partial a}{\partial v_y} \quad \frac{\partial a}{\partial v_z} \right)^{-1} \quad (12)$$

$$Var(a) = \nabla a^T \cdot P \cdot \nabla a \quad (13)$$

It was first assumed that the uncertainty of the SMA would be larger near the region where manoeuvre happened, providing better fitting of the prediction with the operational data. The standard deviation of the SMA was checked and found the densest region left in 0.020149 km as shown in Fig. 18. In the region of the detected manoeuvre, there was no anomalous standard deviation of the SMA. The standard deviation was also vibrating instead of the constant value. By combining the standard deviation (labelled as bars) with the SMA, it was noted that the lowest value happens near the valleys of SMA as shown in Fig. 20. There was no desired symmetry indicating the offset from the lowest standard deviation to the valley of SMA as shown in Fig. 19.

To validate the detection algorithm, 18.9% of the standard deviation less than the threshold of 50 metres were fit with some of the detected manoeuvres using the mean SMA as shown in Fig. 21.

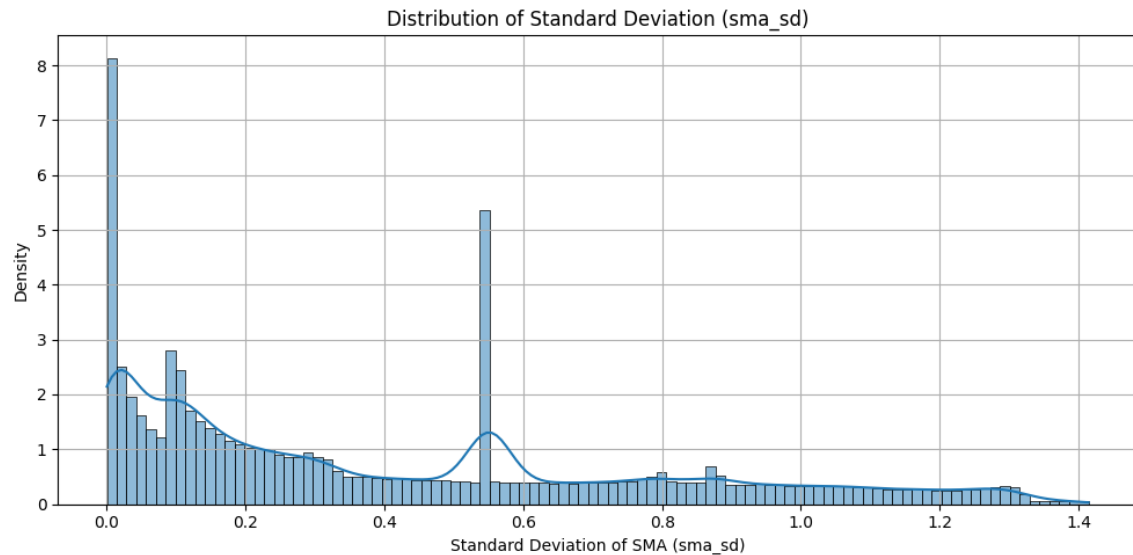


Fig. 18. Distribution of the SMA standard deviation of #61050
 Histogram of Time Offset Between sma_sd and SMA Valleys

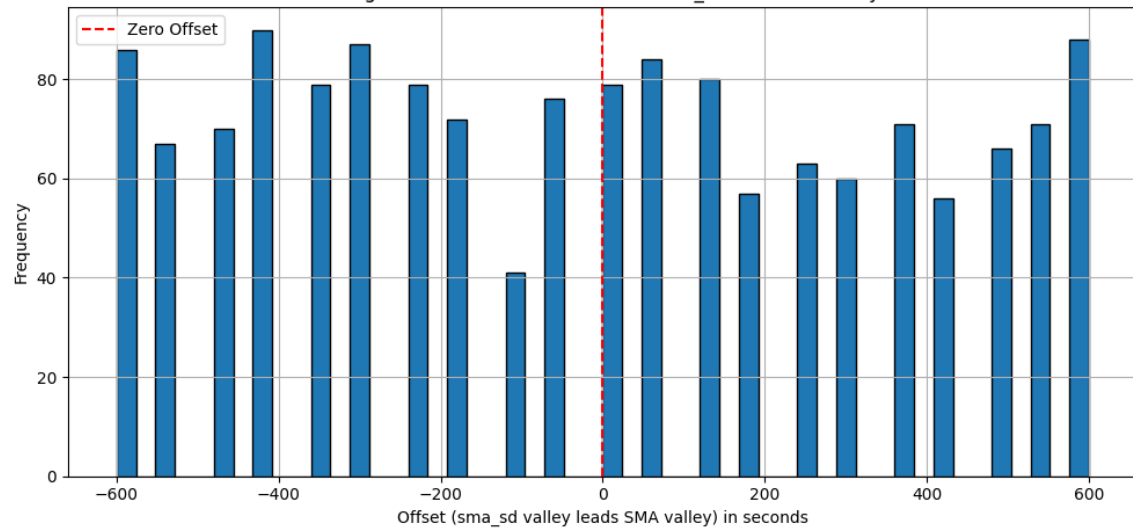


Fig. 19. Time offset between valleys of the standard deviation and the original SMA of #61050

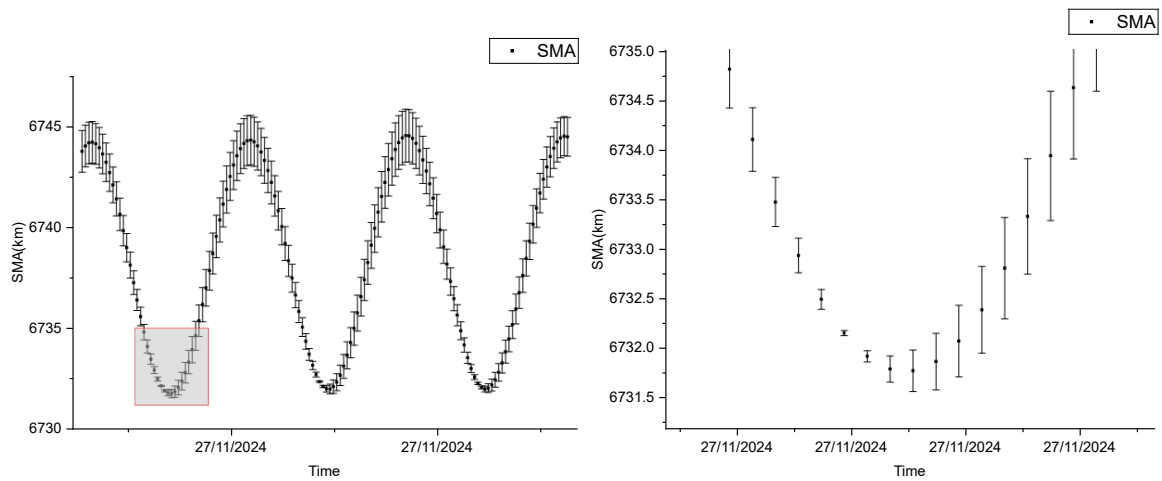


Fig. 20. Original SMA fit with the standard deviation of #61050 (left) with enlarged (right)

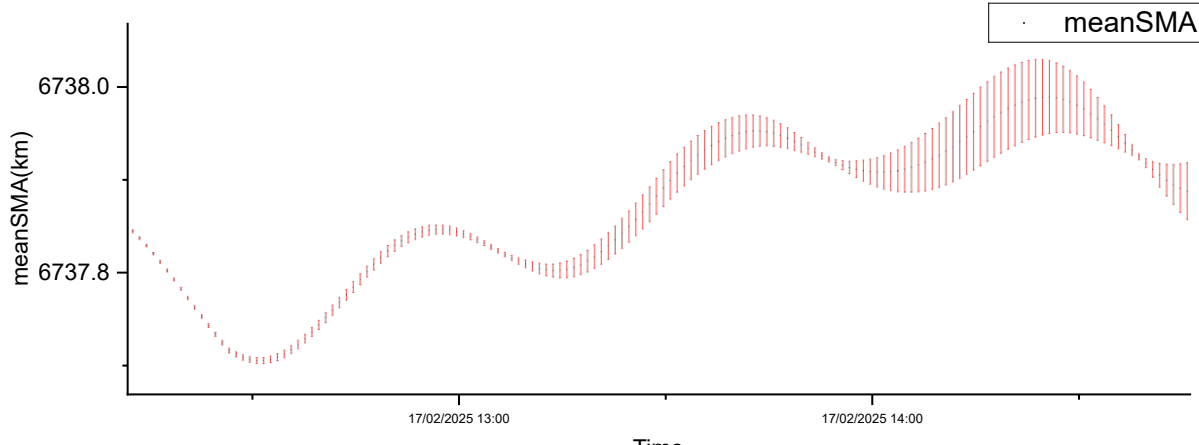


Fig. 21. Validated regions of the detection using the mean SMA

4.2.3 Poincare orbital elements

The Poincare orbital elements (ξ , η , u , v) represented the eccentricity and the argument of perigee, as well as the inclination and the right ascending node, in a vectorized form. This formulation allowed orbital variations to be visualized in a nearly Cartesian coordinate system. Specifically, variations in ξ and η primarily corresponded to in-plane radial or tangential manoeuvres, which could be used to identify changes in SMA or adjustments in the perigee orientation. In contrast, variations in u and v reflected changes in the orbital plane, thereby indicating the direction of normal manoeuvres.

Compared with the traditional Keplerian elements, the Poincare parameters avoided the singularities associated with angular variables, and their numerical trends provided a more direct and stable

characterization of the direction and nature of orbital manoeuvres. After generating the Keplerian orbital elements of the satellites, these values were subsequently transformed into Poincare variables, and two corresponding plots were produced.

Fig. 22 illustrates the plots of ξ , η and u , v for satellite No. 61050 over three consecutive rotational periods of 93 minutes each. The first 93-minute interval is shown in black, the second in red, and the third in green. It is noted that the positions at the same epoch across different cycles exhibited slight deviations. However, after calculating the differences of ξ , η and u , v between corresponding points within each 93-minute interval, no significant variations were detected. Therefore, the analysis of simple point-to-point differences in the Poincare elements was insufficient to capture station-keeping manoeuvres.

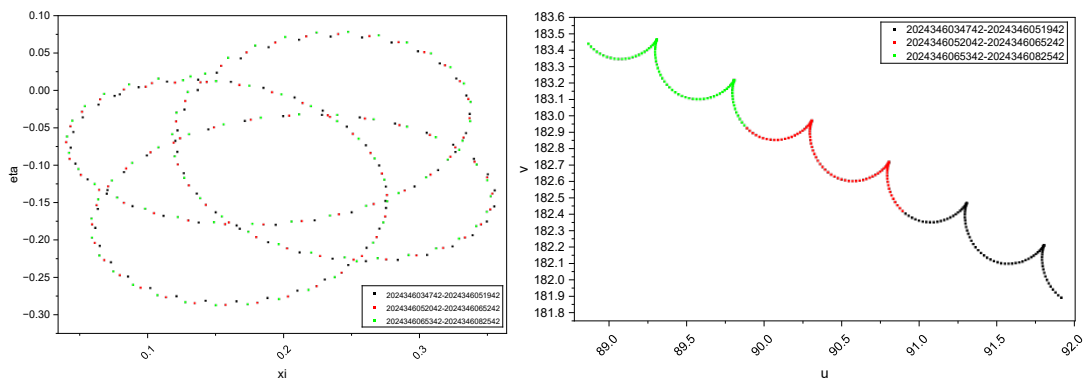


Fig. 22. Visualized results of Poincare orbital elements within three 93-min duration

4.2.4 Machine learning

Since the performance of station-keeping manoeuvres is different among satellites and the covariance provided by the EPH was not aligned with all detected cases, the method with patterns of different manoeuvres recognized by the unsupervised ML and the model for prediction trained by the supervised ML was implemented. Continuous orbital raises were extracted to identify the station-keeping manoeuvre. With features defined as the change of SMA, the

duration of the orbital raise, the speed of the altitude change, and the time interval since last raise, orbital raises were clustered by DBSCAN as shown in Fig. 24. cluster -1 would be the multi-stage deployment manoeuvre and cluster 0 would be the normal operation. According to the characteristic of station-keeping manoeuvres, the magnitude of orbital change and the velocity should be greater than the performance in normal oscillation. By checking the distribution of the two selected features as shown in

Fig. 23, cluster 0, 1 and 2 had similar altitude change with greater velocity happened in cluster 2, which should be the suspected station-keeping manoeuvre. With the missing data and repeated count eliminated,

cluster 2 was restructured by the interval between two cases as shown in Fig. 25. It was found that most suspected manoeuvres were conducted every 5, 10, and 15 hours.

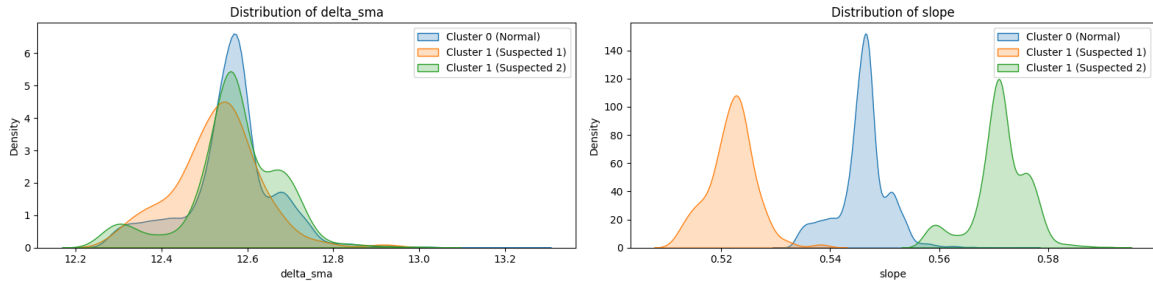


Fig. 23. Performance comparison between the suspected clusters with the normal oscillation

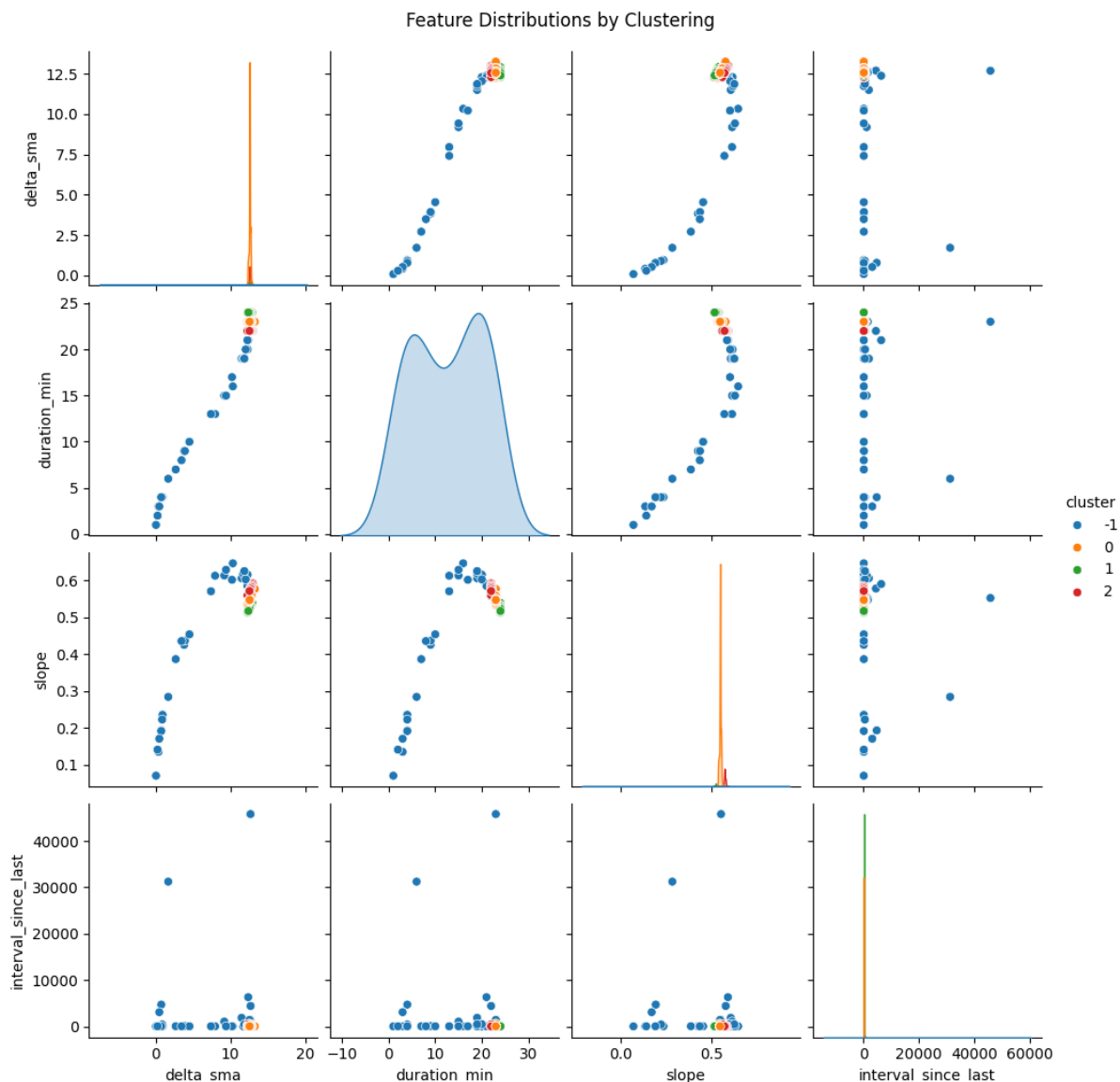


Fig. 24. Clusters of orbital raises processed by DBSCAN

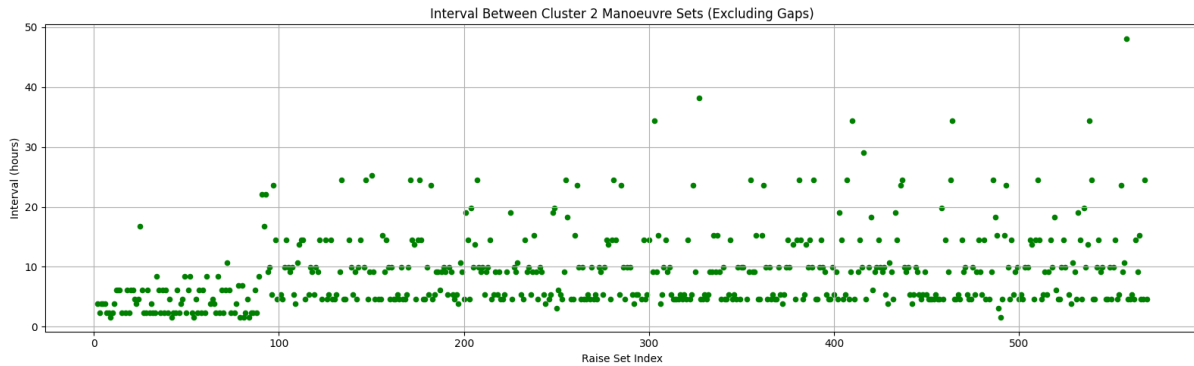


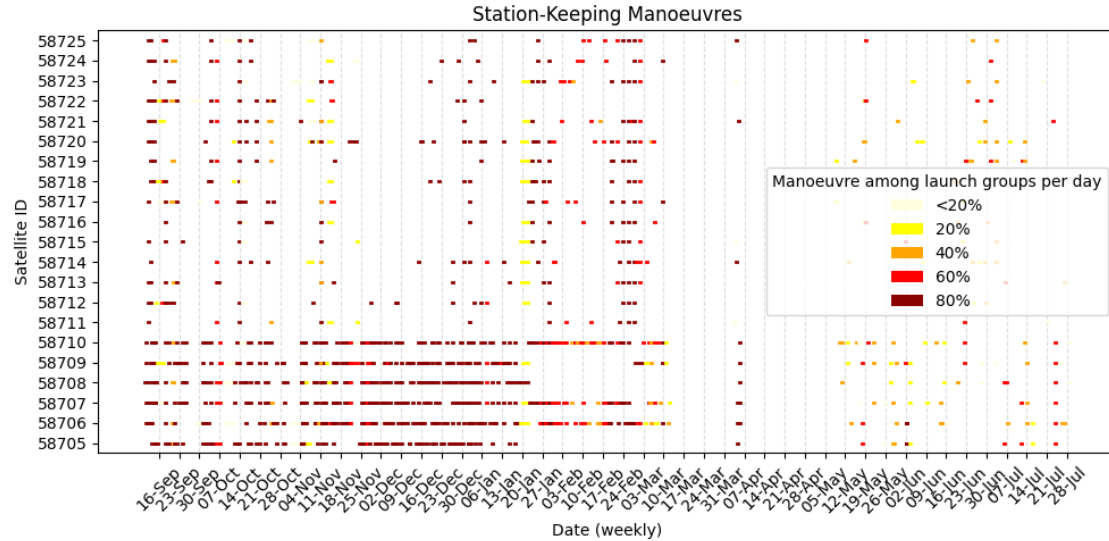
Fig. 25. Intervals between adjacent orbital raises in the suspected cluster

5. Discussion

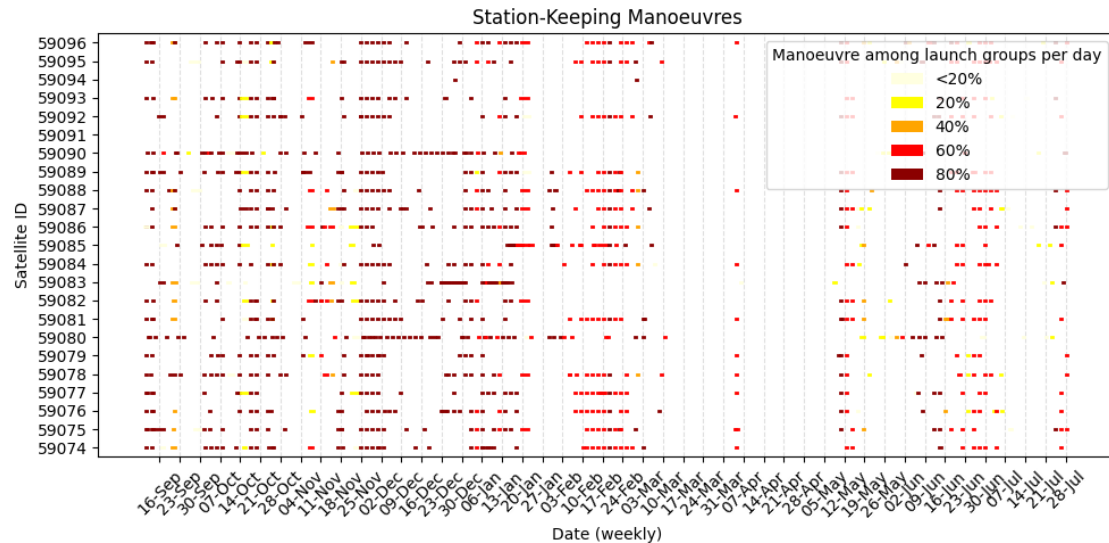
5.1 Result comparison

The algorithm of station-keeping manoeuvre detection was implemented among groups (Launch 133, 144 and 172) of satellites launched on the same

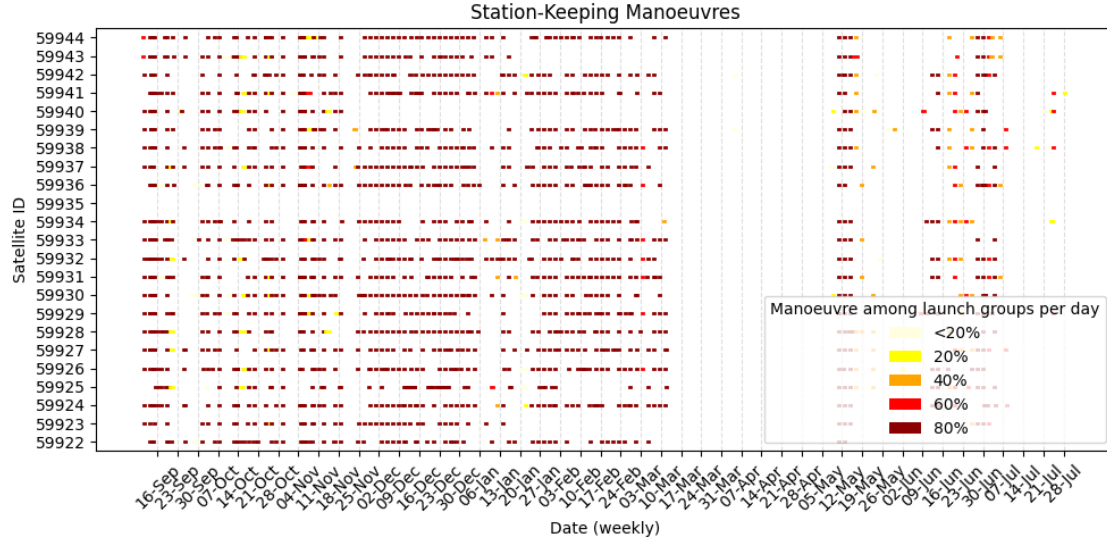
date. Regions of high intensity where most satellites conducting the detected manoeuvre on the same day were labelled in Fig. 26, indicating the integrated adjustment of satellites within the launch group.



(a) Launch 133 (2024-022) #58705-58725



(b) Launch 144 (2024-041) #59074-59096



(c) Launch 172 (2024-106) #59922-59944
 Fig. 26. Line heatmap of detected manoeuvres within launch groups

Other prediction types of orbital performance, such as TLE, were implemented to validate the result of EPH. Sets of TLE, updated twice per day, were propagated into the form of EPH to fit with the sinusoid oscillation as shown in Fig. 27. Since the in-track error of the TLE predicted altitude is generally around 500 metres and would increase along the propagation time [21], it could not validate the detected manoeuvres which was based on the altitude raise of 100 metres.

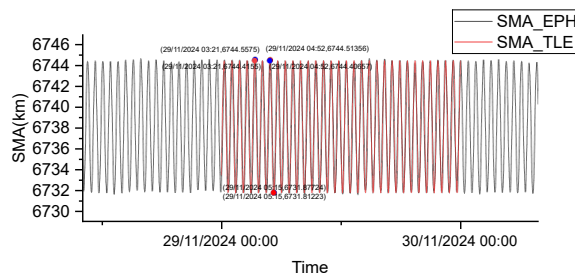


Fig. 27. Comparison of the altitude oscillation from original EPH and TLE-generated EPH

5.2 Future work

The dataset represented predictions and forecasts for the subsequent three days, which raises concerns about its accuracy. The detected manoeuvres should be validated by more robust sources such as the thruster performance, real observational data, and precise manoeuvre handbook from operators.

Considering that the validation sources would be confidential, machine learning discussed in Section 4.2.4 would be suggested to validate the detected manoeuvres with other types identified and learnt by the unsupervised ML. With all patterns such as deployment, deorbiting, station-keeping, and collision-avoidance manoeuvres clustered, supervised model should be generated to compare the detected results

and predict the future performance of satellites in the more crowded LEO space.

As discussed in Section 3.4.3, with the first- and second-order noise correlated from the position and velocity vectors according to the gravitational field, the oscillation amplitude of both SMA and its covariance should be reduced for better detection performance.

The present study focused only on the Poincare orbital parameters and 6COEs. Future research will explore the applicability of other orbital element sets for manoeuvre characterization.

6. Conclusion

The exact time epoch and magnitude of altitude changes have been detected for satellites conducting different types of manoeuvres, which would benefit the arrangement of further launches and the integrated control of mega constellation in the crowding outer LEO region. By applying the high-pass filter of peak-to-peak SMA, deployment and deorbiting manoeuvres were effectively detected and validated through comparison with official records. For station-keeping manoeuvres, detection methods were proposed based on the mean SMA and ML with epochs of suspected manoeuvres identified among satellites grouped by the launch date. Although covariance and clusters of suspected manoeuvres different from normal orbital raises were attempted to verify the detection result, records from operators and observational data would be preferred as validation.

Reference

- [1] STARLINK. <https://www.starlink.com.au> (accessed: 01.09.25)
- [2] S. Cakaj, "The Parameters Comparison of the ‘Starlink’ LEO Satellites Constellation for Different Orbital Shells", *Frontiers in*

- Communications and Networks*, Original Research vol. Volume 2 - 2021, 2021/05/07/ 2021.
- [3] H. Zhi, X. Jiang, and J. Wang, "Multicolour photometry of LEO mega-constellations Starlink and OneWeb," *Monthly Notices of the Royal Astronomical Society*, vol. 530, no. 4, pp. 5006-5015, 2024.
 - [4] D. P. Shorten, W. Karunarathne, and M. Roughan, "How is Starlink manoeuvring? An analysis of patterns in the manoeuvres of Starlink satellites," in Proc. Int. Conf. Internet Things, Big Data Secur., Angers, France, 2024, pp. 174-184.
 - [5] Jonathan McDowell. Jonathan's Space Pages. <https://www.planet4589.org/space/con/star/stats.html> (accessed: 01.09.25)
 - [6] D. P. Shorten, Y. Yang, J. Maclean, and M. Roughan, "Wide-Scale Monitoring of Satellite Lifetimes: Pitfalls and a Benchmark Dataset," *Journal of Spacecraft and Rockets*, vol. 60, no. 6, pp. 2003-2007, 2023.
 - [7] Y. Xu, Y. Zhang, and L. Fan, "Autonomous semi-major axis adjustment for mega constellation continuous coverage," *Advances in Space Research*, vol. 73, no. 11, pp. 5582-5594, 2024/06/01/ 2024.
 - [8] U. Walter, "Orbit Perturbations," in *Astronautics: The Physics of Space Flight*. Cham: Springer Nature Switzerland, 2024, pp. 657-784.
 - [9] T. Li, K. Li, and L. Chen, "New manoeuvre detection method based on historical orbital data for low Earth orbit satellites," *Advances in Space Research*, vol. 62, no. 3, pp. 554-567, 2018/08/01/ 2018.
 - [10] S. Lemmens and H. Krag, "Two-Line-Elements-Based Maneuver Detection Methods for Satellites in Low Earth Orbit," *Journal of Guidance, Control, and Dynamics*, vol. 37, no. 3, pp. 860-868, 2014.
 - [11] J. Kovalevsky, "Tidal effects and the motion of a satellite," *Celestial mechanics*, vol. 34, no. 1, pp. 243-244, 1984/09/01/ 1984.
 - [12] X. Zhou, T. Qin, M. Ji, and D. Qiao, "A LSTM assisted orbit determination algorithm for spacecraft executing continuous maneuver," *Acta Astronautica*, vol. 204, pp. 568-582, 2023/03/01/ 2023.
 - [13] A. Liu, X. Xu, Y. Xiong, and S. Yu, "Maneuver strategies of Starlink satellite based on SpaceX-released ephemeris," *Advances in Space Research*, vol. 74, no. 7, pp. 3157-3169, 2024/10/01/ 2024.
 - [14] SPACE-TRACK.ORG. <https://www.space-track.org/#publicFiles> (accessed: 17.07.25)
 - [15] SPACE-TRACK.ORG. Spaceflight safety handbook for satellite operators. https://www.space-track.org/documents/SFS_Handbook_For_Operators_V1.7.pdf (accessed: 09.09.25)
 - [16] G. R. Hintz, "Survey of Orbit Element Sets," *Journal of Guidance, Control, and Dynamics*, vol. 31, no. 3, pp. 785-790, 2008.
 - [17] Z. W. Sun, W. C. Zhong, S. J. Zhang, and S. Y. Lin, "Real-time onboard estimation of quasi-mean orbital elements based on recursive filter," vol. 34, pp. 1231-1238, 09/01 2013.
 - [18] F. L. Markley and J. L. Crassidis, "Correction to: Fundamentals of Spacecraft Attitude Determination and Control," in *Fundamentals of Spacecraft Attitude Determination and Control*. New York, NY: Springer New York, 2014, pp. C1-C7.
 - [19] National Geospatial-Intelligence Agency, EGM 2008. <https://earth-info.nga.mil> (accessed: 01.09.25)
 - [20] N2YO.com. <https://www.n2yo.com> (accessed: 01.09.25)
 - [21] X.-l. Xu and Y.-q. Xiong, "Orbit error characteristic and distribution of TLE using CHAMP orbit data," *Astrophysics and Space Science*, vol. 363, p. 31, 2018/02/01/ 2018.